A Fluctuating Lattice Boltzmann Model with Independent Directional Stochastic Fluctuations for Brownian Motion

Hongbing Yang[a,b](杨宏兵), Qin Xu[a,b](许钦), Yunye Liu[a,b,*] (刘昀晔), Binghai Wen[a,b,*](闻炳海)

[a]*Key Lab of Education Blockchain and Intelligent Technology, Ministry of Education, Guangxi Normal University, Guilin, 541004, China*

[b]*Guangxi Key Lab of Multi-Source Information Mining and Security, Guangxi Normal University, Guilin 541004, China*

Abstract

Accurate simulation of Brownian motion is essential for understanding particle dynamics at micro- and nanoscales. The fluctuating lattice Boltzmann method provides a mesoscopic framework for modeling thermal fluctuations, but conventional formulations impose identical fluctuations on opposite lattice directions, limiting independent stochastic variation. Here, we relax this symmetry by allowing independent fluctuations in each direction. Formulations are derived for the D3Q19 and D3Q27 models and applied to spherical Brownian particles, with comparisons against the conventional D3Q15 model. The simulated translational and rotational mean-square velocities are consistent with the energy equipartition theorem, confirming thermal equilibrium. The resulting diffusion coefficients demonstrate that the D3Q19 and D3Q27 models reduce the relative error by approximately 3% compared with the D3Q15 model when reproducing the Stokes-Einstein prediction. To quantify inherent errors, a correction factor α is introduced to rescale the fluctuation intensity so that the Stokes-Einstein diffusion coefficient is recovered within statistical uncertainty. The smaller α values required for the D3Q19 and D3Q27 models indicate more physically faithful stochastic behavior. The proposed methods therefore provide a more flexible and accurate representation of thermal fluctuations for Brownian motion and related microscale simulations.

Keywords: Brownian motion; fluctuating lattice Boltzmann method; thermal equilibrium; diffusion coefficient; fluctuation intensity

[*] Corresponding authors.

E-mail: oceanwen@gxnu.edu.cn; 1126785453@qq.com;

PACS: 05.40.Jc, 47.11.Qr, 05.20.-y, 66.10.cg, 05.40.-a

1. Introduction

Brownian motion[1-3] refers to the random thermal motion of microscopic particles suspended in a fluid, arising from continuous collisions between the particles and surrounding fluid molecules. As a classical phenomenon in statistical physics[4], Brownian motion provides an important basis for understanding particle-fluid interactions, thermal noise, and transport processes at the micro- and nanoscales. It is also closely associated with a wide range of applications, including microfluidics[5], biophysics, colloid science[6], and the transport of nanomaterials[7]. Therefore, accurate theoretical modeling and numerical simulation of Brownian motion are essential for revealing the dynamic behavior of suspended particles and for developing predictive tools for relevant engineering applications. Despite its seemingly simple random-walk behavior, Brownian motion involves complex coupling among particle motion, hydrodynamic response, and thermal fluctuations[8, 9] in the surrounding fluid. The central challenge in numerical modeling lies not only in generating random particle trajectories, but also in ensuring that the fluctuation intensity, momentum exchange[10], and dissipative mechanisms remain physically consistent. Among the various numerical approaches, the lattice Boltzmann method[11-13] (LBM) has attracted considerable attention owing to its mesoscopic nature and its ability to describe complex particle-fluid coupled systems.

Traditional numerical approaches for simulating Brownian motion mainly include Brownian dynamics[14] and Stokesian dynamics[15, 16]. Brownian dynamics usually combines the Langevin equation[17, 18] with stochastic force terms to describe the random motion of particles. However, in its conventional form, the flow field is not explicitly resolved, and the feedback effect of particle motion on the surrounding fluid is often simplified or neglected. Stokesian dynamics can account for hydrodynamic interactions among particles more accurately, but its computational cost increases significantly for complex geometries, multiparticle systems, and unsteady flows. These limitations make it challenging for conventional methods to simultaneously capture thermal fluctuations, particle-fluid coupling, and complex flow structures with high computational efficiency. To further account for thermal fluctuations, fluctuating hydrodynamics was proposed by Landau and Lifshitz and was later developed into the

theory of hydrodynamical fluctuations[19]. This theoretical framework provides a bridge between microscopic molecular agitation[20] and macroscopic hydrodynamic behavior and has become an important foundation for fluctuating lattice Boltzmann[21, 22] (FLB) models. Such simulations have been used to study nanoparticle Brownian motion and hydrodynamic interactions under both quiescent and flow conditions. Compared with approaches that directly impose stochastic forces on particles, the FLB method incorporates a fluctuation term into the lattice Boltzmann equation, allowing thermal fluctuations to be transmitted through the mesoscopic fluid field. Consequently, the random motion of suspended particles can be generated naturally through particle-fluid coupling, providing a more physically consistent framework for Brownian motion simulations.

In the FLB model proposed by Nie et al.[23] for the D3Q15 lattice, the fluctuation terms satisfying the fluctuation-dissipation theorem[24] (FDT) are introduced into the lattice Boltzmann evolution equations. A Chapman-Enskog[25] multiscale expansion is then applied to recover the macroscopic hydrodynamic equations, thereby establishing the relationship between the stochastic stress and these fluctuation terms. To obtain explicit expressions for the fluctuation terms, an additional symmetry constraint is imposed: fluctuation terms along symmetry-equivalent lattice directions are set equal. However, the accuracy of an FLB model depends strongly on how the fluctuation terms are constructed at the discrete velocity level. From a physical perspective, molecular thermal motion[26] is inherently stochastic, and the instantaneous fluctuations associated with different discrete velocity directions need not be strictly identical. This strict symmetry constraint simplifies the derivation and helps satisfy conservation laws, but it also constrains the independent variation of stochastic fluctuations across different velocity directions. Therefore, a more flexible construction of fluctuation terms is desirable, particularly for three-dimensional velocity models, to preserve the required conservation laws while providing a more faithful representation of the stochastic nature of Brownian motion.

To address this issue, this paper proposes an improved FLB framework for simulating the Brownian motion of microparticles. The framework builds upon Nie's derivation and introduces a new construction strategy to derive explicit fluctuation terms without enforcing equality between terms in symmetric lattice directions. Independent random numbers are introduced for opposite lattice directions, allowing their fluctuation amplitudes to vary independently. FLB formulations based on the

D3Q19 and D3Q27 three-dimensional velocity models are developed, and explicit expressions for the fluctuation terms in all lattice directions are systematically derived. In contrast to the conventional D3Q15 formulation, the proposed D3Q19 and D3Q27 models no longer impose strict equality between fluctuation terms associated with opposite lattice directions. Thus, the two terms in each symmetric pair can vary independently.

In this paper, the hydrodynamic performance of the proposed models is first validated through classical benchmarks including sedimentation and inertial migration. The models are subsequently applied to simulate the Brownian motion of a spherical particle in a cubic domain. With Nie's conventional D3Q15 model as a reference, the fluctuation behaviors of the D3Q19 and D3Q27 FLB models are evaluated in terms of the energy equipartition theorem[27], mean-square displacement (MSD), and diffusion coefficient[28] (D). The value of D obtained from these models for the spherical particle is compared with the Stokes-Einstein[29] theoretical prediction. The results demonstrate that both the D3Q19 and D3Q27 FLB models yield closer agreement with theoretical expectations compared with the conventional D3Q15 FLB model, corresponding to an approximately 3 % reduction in relative error. To quantify the deviation, a fluctuation intensity correction factor α is further introduced. It is found that the correction factors α required for the D3Q19 and D3Q27 models are smaller than the correction factors α required for the D3Q15 formulation, thereby indicating greater physical fidelity.

2. Numerical Method and Fluctuating Lattice Boltzmann Model

2.1 Lattice Boltzmann method

The lattice Boltzmann method is widely used in fluid dynamics simulations. Compared with traditional methods, it offers several advantages, including a simplified description of fluid interactions, convenient treatment of complex boundaries, strong parallel computing capability, and straightforward implementation. The lattice Boltzmann method typically involves three key elements: the discrete velocity model[30], the equilibrium distribution function, and the evolution equation for the distribution function. This method fully discretizes velocity, time, and space, performing collision and streaming steps in the discretized phase space. The

single-relaxation-time lattice Boltzmann equation is as follows:

$$f_i(\boldsymbol{x}+\boldsymbol{e}_i\delta_t,t+\delta_t)=f_i(\boldsymbol{x},t)-\frac{1}{\tau}[f_i(\boldsymbol{x},t)-f_i^{eq}(\boldsymbol{x},t)], \tag{1}$$

where $f_i(x,t)$ denotes the density distribution function at grid point x and time t along the discrete velocity direction i; τ refers to the relaxation time; $f_i^{eq}(x,t)$ refers to the distribution function in the equilibrium state, which can be written as

$$f_i^{eq}(\boldsymbol{x},t)=\rho\omega_i[1+\frac{\boldsymbol{e}_i\cdot\boldsymbol{u}}{c_s^2}+\frac{(\boldsymbol{e}_i\cdot\boldsymbol{u})^2}{2c_s^4}-\frac{\boldsymbol{u}^2}{2c_s^2}], \tag{2}$$

where $\rho=\sum_i f_i$ and $\frac{1}{\rho}\sum_i e_i f_i$ represent the density and velocity of the fluid points; u is the fluid velocity; ω_i is the weight factor, which varies in different directions depending on the velocity model. The lattice sound speed is $c_s=c/\sqrt{3}$, where $c=\delta_x/\delta_t$, and δ_x and δ_t are the spatial and temporal steps, respectively. This paper adopts three widely used discrete velocity models within the standard DdQm framework proposed by Qian et al.[31], namely D3Q15, D3Q19, and D3Q27. Figure 1 visually illustrates the distribution of discrete velocity vectors in three-dimensional space for each model. In a three-dimensional grid with a D3Q15 velocity model, the weight factors in each direction are $\omega_0=2/9$, $\omega_{1-6}=1/9$, and $\omega_{7-14}=1/72$. The discretized velocity is

$$\boldsymbol{e}=\begin{bmatrix}0&1&-1&0&0&0&0&1&-1&1&-1&1&-1&-1&1\\0&0&0&1&-1&0&0&1&-1&1&-1&-1&1&1&-1\\0&0&0&0&0&1&-1&1&-1&-1&1&1&-1&1&-1\end{bmatrix}. \tag{3}$$

For the D3Q19 three-dimensional velocity model, the weight factors in each direction are $\omega_0=1/3$, $\omega_{1-6}=1/18$, and $\omega_{7-18}=1/36$. The velocity model is

$$\boldsymbol{e}=\begin{bmatrix}0&1&-1&0&0&0&0&1&-1&1&-1&1&-1&1&-1&0&0&0&0\\0&0&0&1&-1&0&0&1&-1&-1&1&0&0&0&0&1&-1&1&-1\\0&0&0&0&0&1&-1&0&0&0&0&1&-1&-1&1&1&-1&-1&1\end{bmatrix}. \tag{4}$$

For the D3Q27 three-dimensional velocity model, the weight factors in each direction are $\omega_0=8/27$, $\omega_{1-6}=2/27$, and $\omega_{7-18}=1/54$ and $\omega_{19-26}=1/216$. The corresponding velocity set is

$$\boldsymbol{e}=\begin{bmatrix}0&1&-1&0&0&0&0&1&-1&1&-1&-1&1&0&0&-1&1&0&0&-1&1&-1&1&1&-1&-1&1\\0&0&0&1&-1&0&0&1&-1&-1&1&0&0&1&-1&0&0&-1&1&1&-1&-1&1&1&-1&1&-1\\0&0&0&0&0&-1&1&0&0&0&0&-1&1&1&-1&1&-1&1&-1&1&-1&-1&1&-1&1&-1&1\end{bmatrix}. \tag{5}$$

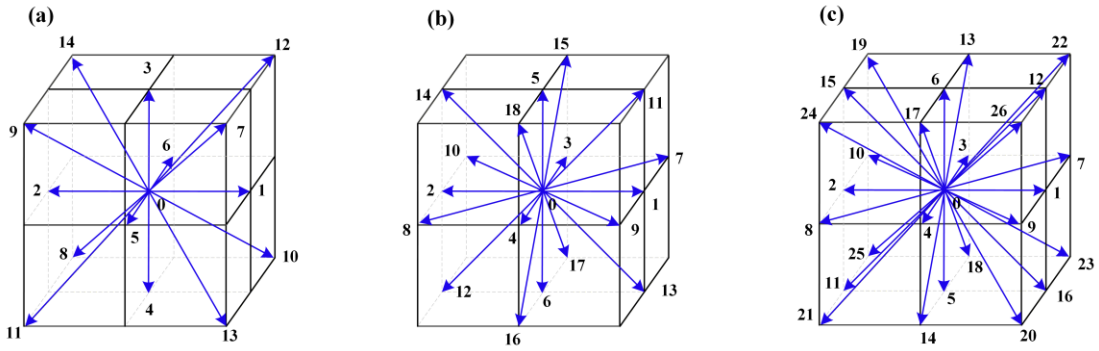


Figure 1: (a), (b), and (c) are schematic diagrams of the D3Q15, D3Q19, and D3Q27 3D velocity models, respectively

At each time step, the evolution of the lattice Boltzmann equation can be divided into two steps: collision and streaming, which can be written as follows:

$$\text{Collision:} \quad \tilde{f}(x,t) = -\frac{1}{\tau}[f_i(x,t) - f_i^{eq}(x,t)], \tag{6}$$

$$\text{Streaming:} \quad f_i(x + e_i\delta_t, t + \delta_t) = \tilde{f} \tag{7}$$

Here, f_i and $\tilde{f}_i$ represent the density distribution functions in the pre-collision and post-collision states at the current grid point, respectively. Since the collision step accounts for the majority of the computation and is fully local, it is suitable for parallelization.

2.2 The single-relaxation fluctuating lattice Boltzmann model

The single-relaxation FLB method adds a fluctuation term to the fully discretized lattice Boltzmann (BGK[32, 33]) equation, so that the evolution equation is written as follows:

$$f_i(\boldsymbol{x} + \boldsymbol{e}_i\delta_t, t + \delta_t) = f_i(\boldsymbol{x},t) - \frac{1}{\tau}[f_i(\boldsymbol{x},t) - f_i^{eq}(\boldsymbol{x},t)] + f_i^f, \tag{8}$$

where f_i^f represents the fluctuations caused by molecular thermal motion, satisfying the conservation of mass and momentum:

$$\sum f_i^f = 0 \quad , \quad \sum f_i^f \boldsymbol{e}_i = 0. \tag{9}$$

By using the Chapman-Enskog multiscale expansion, the macroscopic fluid dynamics equations can be derived from Eq. (8):

$$\partial_t \rho + \partial_\alpha(\rho \boldsymbol{u}_\alpha) = 0, \tag{10}$$

$$\partial_t(\rho \boldsymbol{u}_\alpha) + \partial_\beta(\rho \boldsymbol{u}_\alpha \boldsymbol{u}_\beta) = -\partial_\alpha P + \upsilon\partial_\beta[\partial_\alpha(\rho \boldsymbol{u}_\beta) + \partial_\beta(\rho \boldsymbol{u}_\alpha)] + \partial_\beta \sigma_{\alpha\beta}^f. \tag{11}$$

In the equation, the values of α, β and γ can be x , y or z, and $\upsilon = c_s^2(\tau -$

1/2). Compared with the standard Navier-Stokes equations[34], Eq. (11) includes an additional term $\sigma_{\alpha\beta}^{f}$, which represents the stochastic stress term in fluctuation dynamics. In the process of deriving the macroscopic fluid motion equations from the lattice Boltzmann evolution equations, a relationship between $\sigma_{\alpha\beta}^{f}$ and fluctuation terms can be obtained:

$$\sigma_{\alpha\beta}^{f} = -\tau \sum_{i} e_{i\alpha} e_{i\beta} f_{i}^{f}. \tag{12}$$

Eq. (11) relates the stochastic stress tensor in the Navier-Stokes equations to the fluctuation term in Eq. (8). The values of the stochastic stress tensor $\sigma_{\alpha\beta}^{f}$ are determined together by the relaxation time τ, the velocity model, and the fluctuation term f_i^f. According to the Landau and Lifshitz theory[35] of fluctuating hydrodynamics, for an incompressible fluid, the stochastic stress tensor $\sigma_{\alpha\beta}^{f}$ satisfies the following conditions:

$$< \sigma_{\alpha\beta}^{f} > = 0, \tag{13}$$

$$< \sigma_{\alpha\beta}^{f}(\boldsymbol{x}_1, t_1) \sigma_{\gamma\delta}^{f}(\boldsymbol{x}_2, t_2) > = 2k_B T \mu (\delta_{\alpha\gamma}\delta_{\beta\delta} + \delta_{\alpha\delta}\delta_{\beta\gamma} - \frac{2}{3}\delta_{\alpha\beta}\delta_{\gamma\delta}) \delta(\boldsymbol{x}_1 - \boldsymbol{x}_2) \delta(t_1 - t_2), \tag{14}$$

where k_B is the Boltzmann constant, T is the absolute temperature of the fluid, μ is the dynamic viscosity coefficient of the fluid, and the values of α, β and γ can be x, y or z.

This study considers three 3D velocity models, D3Q15, D3Q19, and D3Q27, each of which corresponds to a distinct FLB model. For the D3Q15 FLB model, Nie's symmetry assumption is adopted, which states that for every pair of opposite lattice directions, the two corresponding fluctuation terms f_i^f are equal. By further solving Eqs. (9) and (12), the expressions for fluctuation terms f_i^f in each direction can be obtained. The expressions of fluctuation terms in each direction can be written as:

$$
\begin{aligned}
f_0^f &= 0, \\
f_1^f &= f_2^f = \frac{\sigma_{yy}^f + \sigma_{zz}^f}{2\tau}, \\
f_3^f &= f_4^f = \frac{\sigma_{xx}^f + \sigma_{zz}^f}{2\tau}, \\
f_5^f &= f_6^f = \frac{\sigma_{xx}^f + \sigma_{yy}^f}{2\tau}, \\
f_7^f &= f_8^f = \frac{\sigma_{xx}^f + \sigma_{yy}^f + \sigma_{zz}^f + \sigma_{xy}^f + \sigma_{yz}^f + \sigma_{xz}^f}{8\tau}, \\
f_9^f &= f_{10}^f = \frac{\sigma_{xx}^f + \sigma_{yy}^f + \sigma_{zz}^f - \sigma_{xy}^f + \sigma_{yz}^f - \sigma_{xz}^f}{8\tau}, \\
f_{11}^f &= f_{12}^f = \frac{\sigma_{xx}^f + \sigma_{yy}^f + \sigma_{zz}^f + \sigma_{xy}^f - \sigma_{yz}^f - \sigma_{xz}^f}{8\tau}, \\
f_{13}^f &= f_{14}^f = \frac{\sigma_{xx}^f + \sigma_{yy}^f + \sigma_{zz}^f - \sigma_{xy}^f + \sigma_{yz}^f + \sigma_{xz}^f}{8\tau}.
\end{aligned} \tag{15}
$$

It is worth emphasizing that the construction of the fluctuation terms differs among the models adopted here. Specifically, the D3Q15 FLB model strictly follows the original symmetry assumption established by Nie et al.[36] and serves as the baseline for comparison. In contrast, the formulations for the D3Q19 and D3Q27 FLB models presented in this work are our original contributions. For these two models, the strict symmetry constraint is relaxed by allowing independent stochastic variations in opposite directions, while preserving the required conservation laws through constrained sums. This relaxation constitutes the primary algorithmic novelty of the present study.

Once the constraints given by Eqs. (9) and (12) are enforced, an additional closure principle is required to determine the fluctuation term in each direction. Based on the structure of Eqs. (9) and (12), it follows that, when the explicit expressions of the fluctuation terms are solved, the sums and differences of the fluctuation terms along symmetric directions consistently appear in pairs. This observation suggests that the conventional symmetry assumption $f_{2i-1}^f = f_{2i}^f$ is a sufficient but not necessary condition for satisfying Eqs. (9) and (12). For the D3Q19 FLB model, the present formulation sets $f_{2i-1}^f + f_{2i}^f = \xi_i$, where i = 1, 2, …, 9. To obtain a theoretical solution, the sums over the three groups of secondary diagonal directions are assumed equal, that is $\xi_5 = \xi_7 = \xi_9$. Based on the mass conservation equation and Eq. (12), the fluctuations in the nine symmetric directions, denoted ξ_i, i = 1, 2, …, 9, can then be

uniquely determined. Setting $f_{2i-1}^{f} - f_{2i}^{f} = \varepsilon_i$, where i = 1, 2, …, 9, and substituting these into the equations for momentum conservation in the three directions yields 9 sets of solutions for the difference between symmetric directional fluctuations ε_i, i = 1, 2, …, 9, involving 6 free variables. The six free variables are obtained by solving the linear system of three momentum equations (in the x, y and z directions) for ε_i. In the resulting solution, ε_4 through ε_9 are expressed in terms of the free variables, while ε_1 through ε_3 are expressed in terms of ξ_4 through ξ_9. In this way, the strong symmetry constraints of the traditional D3Q15 FLB model can be relaxed. From the sum and difference of the fluctuations in the symmetric directions, the following expression is obtained:

$$
\begin{aligned}
&f_0^f = 0,\\
&f_1^f = \frac{-\sigma_{xx} + 2\sigma_{yy} + 2\sigma_{zz} + \sigma_{xy} + \sigma_{xz} - 2\sigma_{yz}}{6\tau} + \frac{-\lambda_1 - \lambda_2 - \lambda_3 - \lambda_4}{2},\\
&f_2^f = \frac{-\sigma_{xx} + 2\sigma_{yy} + 2\sigma_{zz} + \sigma_{xy} + \sigma_{xz} - 2\sigma_{yz}}{6\tau} - \frac{-\lambda_1 - \lambda_2 - \lambda_3 - \lambda_4}{2},\\
&f_3^f = \frac{2\sigma_{xx} - \sigma_{yy} + 2\sigma_{zz} + \sigma_{xy} - 2\sigma_{xz} + \sigma_{yz}}{6\tau} + \frac{-\lambda_1 + \lambda_2 - \lambda_5 - \lambda_6}{2},\\
&f_4^f = \frac{2\sigma_{xx} - \sigma_{yy} + 2\sigma_{zz} + \sigma_{xy} - 2\sigma_{xz} + \sigma_{yz}}{6\tau} - \frac{-\lambda_1 + \lambda_2 - \lambda_5 - \lambda_6}{2},\\
&f_5^f = \frac{2\sigma_{xx} + 2\sigma_{yy} - \sigma_{zz} - 2\sigma_{xy} + \sigma_{xz} + \sigma_{yz}}{6\tau} + \frac{-\lambda_3 + \lambda_4 - \lambda_5 + \lambda_6}{2},\\
&f_6^f = \frac{2\sigma_{xx} + 2\sigma_{yy} - \sigma_{zz} - 2\sigma_{xy} + \sigma_{xz} + \sigma_{yz}}{6\tau} - \frac{-\lambda_3 + \lambda_4 - \lambda_5 + \lambda_6}{2},\\
&f_7^f = \frac{-\sigma_{xx} - \sigma_{yy} - \sigma_{zz} - 5\sigma_{xy} + \sigma_{xz} + \sigma_{yz}}{12\tau} + \frac{\lambda_1}{2}, \qquad f_8^f = \frac{-\sigma_{xx} - \sigma_{yy} - \sigma_{zz} - 5\sigma_{xy} + \sigma_{xz} + \sigma_{yz}}{12\tau} - \frac{\lambda_1}{2},\\
&f_9^f = \frac{-\sigma_{xx} - \sigma_{yy} - \sigma_{zz} + \sigma_{xy} + \sigma_{xz} + \sigma_{yz}}{12\tau} + \frac{\lambda_2}{2}, \qquad f_{10}^f = \frac{-\sigma_{xx} - \sigma_{yy} - \sigma_{zz} + \sigma_{xy} + \sigma_{xz} + \sigma_{yz}}{12\tau} - \frac{\lambda_2}{2},\\
&f_{11}^f = \frac{-\sigma_{xx} - \sigma_{yy} - \sigma_{zz} + \sigma_{xy} - 5\sigma_{xz} + \sigma_{yz}}{12\tau} + \frac{\lambda_3}{2}, \qquad f_{12}^f = \frac{-\sigma_{xx} - \sigma_{yy} - \sigma_{zz} + \sigma_{xy} - 5\sigma_{xz} + \sigma_{yz}}{12\tau} - \frac{\lambda_3}{2},\\
&f_{13}^f = \frac{-\sigma_{xx} - \sigma_{yy} - \sigma_{zz} + \sigma_{xy} + \sigma_{xz} + \sigma_{yz}}{12\tau} + \frac{\lambda_4}{2}, \qquad f_{14}^f = \frac{-\sigma_{xx} - \sigma_{yy} - \sigma_{zz} + \sigma_{xy} + \sigma_{xz} + \sigma_{yz}}{12\tau} - \frac{\lambda_4}{2},\\
&f_{15}^f = \frac{-\sigma_{xx} - \sigma_{yy} - \sigma_{zz} + \sigma_{xy} + \sigma_{xz} - 5\sigma_{yz}}{12\tau} + \frac{\lambda_5}{2}, \qquad f_{16}^f = \frac{-\sigma_{xx} - \sigma_{yy} - \sigma_{zz} + \sigma_{xy} + \sigma_{xz} - 5\sigma_{yz}}{12\tau} - \frac{\lambda_5}{2},\\
&f_{17}^f = \frac{-\sigma_{xx} - \sigma_{yy} - \sigma_{zz} + \sigma_{xy} + \sigma_{xz} + \sigma_{yz}}{12\tau} + \frac{\lambda_6}{2}, \qquad f_{18}^f = \frac{-\sigma_{xx} - \sigma_{yy} - \sigma_{zz} + \sigma_{xy} + \sigma_{xz} + \sigma_{yz}}{12\tau} - \frac{\lambda_6}{2}.
\end{aligned}
\tag{16}
$$

In Eq. (16), λ_i are free variables, where i = 1, 2, …, 6; f_i^f represents the fluctuation amplitude along direction i; and $\sigma_{\alpha\beta}^f$ denotes the random stress component, where α and β can each take one of the values x, y, or z. All

quantities here are expressed in lattice units, and the free variables share the same dimensions as the fluctuation amplitudes. These random numbers are allowed to vary uniformly within a narrow interval determined by the sum of the fluctuation terms in the symmetric pairs among velocity directions 7 through 18. For example, λ_i is allowed to fluctuate uniformly between $-\frac{1}{10}|\xi_{i+3}|$ and $\frac{1}{10}|\xi_{i+3}|$. The coefficient $1/10$ is used to introduce a moderate perturbation without changing the dominant contribution determined by the symmetric sums. The sum ξ_i enters both the zeroth-order mass moment and the second-order stress moment and is therefore the leading-order quantity that must be strictly enforced. The difference ε_i, by contrast, introduces directional randomness: its components, which are constrained by the momentum conservation equation, are uniquely determined, whereas the remaining ones emerge as free variables λ_i and constitute secondary perturbations. To preserve the leading-order conservation laws, the amplitude of the difference is required to be at least one order of magnitude smaller than the characteristic scale of the sum. In the limit as this coefficient vanishes, the difference terms disappear and the model reduces to the conventional symmetric closure, in which the fluctuations along each pair of opposite lattice directions coincide. At the other extreme, when the coefficient is of order unity, the difference terms become comparable to the symmetric sums. As a result, the perturbative ordering collapses and the leading-order conserved modes are contaminated. The value 1/10 is thus adopted as the standard choice, ensuring that the directional correction remains one order of magnitude below the leading contribution. Because these free variables enter only the first-order momentum moment, they do not appear in the second-order stress moment and hence leave the stress covariance prescribed by the FDT unchanged.

Similarly, for the D3Q27 FLB model, this paper sets $f_{2i-1}^f + f_{2i}^f = \xi_i$, where i = 1, 2, …, 13. To obtain a theoretical solution, this paper makes reasonable assumptions based on the weight coefficients of the D3Q27 lattice model, assuming $\xi_4 = \xi_5 = \frac{1}{4}\xi_1$, $\xi_7 = \xi_9 = \frac{1}{4}\xi_2$, $\xi_6 = \xi_8 = \frac{1}{4}\xi_3$. Then, using the mass conservation equation and Eq. (12), the fluctuations in the 13 symmetric directions ξ_i are uniquely determined. Setting $f_{2i-1}^f - f_{2i}^f = \varepsilon_i$ where i = 1, 2, …, 13, and substituting these into the equations for momentum conservation in the three directions, 13 sets of solutions for the difference between the symmetric directional fluctuations involving

ten free variables are obtained. From the sum and difference of the fluctuations in the symmetric directions, the following expressions are obtained:

$$f_0^f = 0,$$

$$f_1^f = \frac{-6\sigma_{xx} + 4\sigma_{yy} + 9\sigma_{zz}}{35\tau} + \frac{-\varphi_1 - \varphi_2 + \varphi_3 + \varphi_5 + \varphi_7 + \varphi_8 - \varphi_9 + \varphi_{10}}{2},$$

$$f_2^f = \frac{-6\sigma_{xx} + 4\sigma_{yy} + 9\sigma_{zz}}{35\tau} - \frac{-\varphi_1 - \varphi_2 + \varphi_3 + \varphi_5 + \varphi_7 + \varphi_8 - \varphi_9 + \varphi_{10}}{2},$$

$$f_3^f = \frac{9\sigma_{xx} - 6\sigma_{yy} + 4\sigma_{zz}}{35\tau} + \frac{-\varphi_1 + \varphi_2 - \varphi_4 + \varphi_6 - \varphi_7 + \varphi_8 - \varphi_9 - \varphi_{10}}{2},$$

$$f_4^f = \frac{9\sigma_{xx} - 6\sigma_{yy} + 4\sigma_{zz}}{35\tau} - \frac{-\varphi_1 + \varphi_2 - \varphi_4 + \varphi_6 - \varphi_7 + \varphi_8 - \varphi_9 - \varphi_{10}}{2},$$

$$f_5^f = \frac{4\sigma_{xx} + 9\sigma_{yy} - 6\sigma_{zz}}{35\tau} + \frac{-\varphi_3 + \varphi_4 + \varphi_5 + \varphi_6 + \varphi_7 - \varphi_8 - \varphi_9 - \varphi_{10}}{2},$$

$$f_6^f = \frac{4\sigma_{xx} + 9\sigma_{yy} - 6\sigma_{zz}}{35\tau} - \frac{-\varphi_3 + \varphi_4 + \varphi_5 + \varphi_6 + \varphi_7 - \varphi_8 - \varphi_9 - \varphi_{10}}{2},$$

$$f_7^f = \frac{-6\sigma_{xx} + 4\sigma_{yy} + 9\sigma_{zz}}{140\tau} + \frac{\varphi_1}{2}, \qquad f_8^f = \frac{-6\sigma_{xx} + 4\sigma_{yy} + 9\sigma_{zz}}{140\tau} - \frac{\varphi_1}{2},$$

$$f_9^f = \frac{-6\sigma_{xx} + 4\sigma_{yy} + 9\sigma_{zz}}{140\tau} + \frac{\varphi_2}{2}, \qquad f_{10}^f = \frac{-6\sigma_{xx} + 4\sigma_{yy} + 9\sigma_{zz}}{140\tau} - \frac{\varphi_2}{2},$$

$$f_{11}^f = \frac{4\sigma_{xx} + 9\sigma_{yy} - 6\sigma_{zz}}{140\tau} + \frac{\varphi_3}{2}, \qquad f_{12}^f = \frac{4\sigma_{xx} + 9\sigma_{yy} - 6\sigma_{zz}}{140\tau} - \frac{\varphi_3}{2},$$

$$f_{13}^f = \frac{9\sigma_{xx} - 6\sigma_{yy} + 4\sigma_{zz}}{140\tau} + \frac{\varphi_4}{2}, \qquad f_{14}^f = \frac{9\sigma_{xx} - 6\sigma_{yy} + 4\sigma_{zz}}{140\tau} - \frac{\varphi_4}{2},$$

$$f_{15}^f = \frac{4\sigma_{xx} + 9\sigma_{yy} - 6\sigma_{zz}}{140\tau} + \frac{\varphi_5}{2}, \qquad f_{16}^f = \frac{4\sigma_{xx} + 9\sigma_{yy} - 6\sigma_{zz}}{140\tau} - \frac{\varphi_5}{2},$$

$$f_{17}^f = \frac{9\sigma_{xx} - 6\sigma_{yy} + 4\sigma_{zz}}{140\tau} + \frac{\varphi_6}{2}, \qquad f_{18}^f = \frac{9\sigma_{xx} - 6\sigma_{yy} + 4\sigma_{zz}}{140\tau} - \frac{\varphi_6}{2},$$

$$f_{19}^f = -\frac{3\sigma_{xx} + 3\sigma_{yy} + 3\sigma_{zz} - 5\sigma_{xy} - 5\sigma_{xz} + 5\sigma_{yz}}{40\tau} + \frac{\varphi_7}{2},$$

$$f_{20}^f = -\frac{3\sigma_{xx} + 3\sigma_{yy} + 3\sigma_{zz} - 5\sigma_{xy} - 5\sigma_{xz} + 5\sigma_{yz}}{40\tau} - \frac{\varphi_7}{2},$$

$$f_{21}^f = -\frac{3\sigma_{xx} + 3\sigma_{yy} + 3\sigma_{zz} + 5\sigma_{xy} + 5\sigma_{xz} + 5\sigma_{yz}}{40\tau} + \frac{\varphi_8}{2},$$

$$f_{22}^f = -\frac{3\sigma_{xx} + 3\sigma_{yy} + 3\sigma_{zz} + 5\sigma_{xy} + 5\sigma_{xz} + 5\sigma_{yz}}{40\tau} - \frac{\varphi_8}{2},$$

$$f_{23}^f = -\frac{3\sigma_{xx} + 3\sigma_{yy} + 3\sigma_{zz} + 5\sigma_{xy} - 5\sigma_{xz} - 5\sigma_{yz}}{40\tau} + \frac{\varphi_9}{2},$$

$$f_{24}^f = -\frac{3\sigma_{xx} + 3\sigma_{yy} + 3\sigma_{zz} + 5\sigma_{xy} - 5\sigma_{xz} - 5\sigma_{yz}}{40\tau} - \frac{\varphi_9}{2},$$

$$f_{25}^f = -\frac{3\sigma_{xx} + 3\sigma_{yy} + 3\sigma_{zz} - 5\sigma_{xy} + 5\sigma_{xz} - 5\sigma_{yz}}{40\tau} + \frac{\varphi_{10}}{2},$$

$$f_{26}^f = -\frac{3\sigma_{xx} + 3\sigma_{yy} + 3\sigma_{zz} - 5\sigma_{xy} + 5\sigma_{xz} - 5\sigma_{yz}}{40\tau} - \frac{\varphi_{10}}{2}.$$

(17)

Here, φ_i are free variables, where i = 1, 2, …, 10. Solving the linear system of momentum conservation equations in the three directions (for the unknowns ε_i) yields ten free variables. In the resulting solution, ε_4 through ε_{13} are expressed in terms of these free variables, while the values for ε_1 through ε_3 are obtained from ε_4 through ε_{13}. Similar to the D3Q19 FLB model, these free variables are defined as random numbers with specified distributions. They are likewise allowed to fluctuate uniformly within a narrow range, which is related to the sum of the fluctuations in the symmetric pairs among the velocity directions 7 through 26. For instance, φ_i is likewise allowed to fluctuate uniformly between $-\frac{1}{10}|\xi_{i+3}|$ and $\frac{1}{10}|\xi_{i+3}|$, thereby ensuring the randomness of the fluctuations across the 27 directions. This approach to constructing the D3Q19 and D3Q27 models can also be applied to other three-dimensional models, as long as they satisfy Eqs. (9) and (12).

Furthermore, according to FDT, the stochastic stress components must satisfy the following conditions:

$$
\begin{aligned}
&< \sigma_{xx}^f >= 0, < \sigma_{xx}^f \sigma_{xx}^f >= \frac{4}{3}A, < \sigma_{xx}^f \sigma_{yy}^f >=< \sigma_{xx}^f \sigma_{zz}^f >= -\frac{2}{3}A, < \sigma_{xx}^f \sigma_{xy}^f >=< \sigma_{xy}^f \sigma_{xz}^f >=< \sigma_{xx}^f \sigma_{yz}^f >= 0,\\
&< \sigma_{yy}^f >= 0, < \sigma_{yy}^f \sigma_{yy}^f >= \frac{4}{3}A, < \sigma_{yy}^f \sigma_{xx}^f >=< \sigma_{yy}^f \sigma_{zz}^f >= -\frac{2}{3}A, < \sigma_{yy}^f \sigma_{xy}^f >=< \sigma_{yy}^f \sigma_{xz}^f >=< \sigma_{yy}^f \sigma_{yz}^f >= 0,\\
&< \sigma_{zz}^f >= 0, < \sigma_{zz}^f \sigma_{zz}^f >= \frac{4}{3}A, < \sigma_{zz}^f \sigma_{xx}^f >=< \sigma_{zz}^f \sigma_{yy}^f >= -\frac{2}{3}A, < \sigma_{zz}^f \sigma_{xy}^f >=< \sigma_{zz}^f \sigma_{xz}^f >=< \sigma_{zz}^f \sigma_{yz}^f >= 0,\\
&< \sigma_{xy}^f >= 0, < \sigma_{xy}^f \sigma_{xy}^f >= A, < \sigma_{xy}^f \sigma_{xx}^f >=< \sigma_{xy}^f \sigma_{yy}^f >=< \sigma_{xy}^f \sigma_{zz}^f >=< \sigma_{xy}^f \sigma_{xz}^f >=< \sigma_{xy}^f \sigma_{yz}^f >= 0,\\
&< \sigma_{xz}^f >= 0, < \sigma_{xz}^f \sigma_{xz}^f >= A, < \sigma_{xz}^f \sigma_{xx}^f >=< \sigma_{xz}^f \sigma_{yy}^f >=< \sigma_{xz}^f \sigma_{zz}^f >=< \sigma_{xz}^f \sigma_{xy}^f >=< \sigma_{xz}^f \sigma_{yz}^f >= 0,\\
&< \sigma_{yz}^f >= 0, < \sigma_{yz}^f \sigma_{yz}^f >= A, < \sigma_{yz}^f \sigma_{xx}^f >=< \sigma_{yz}^f \sigma_{yy}^f >=< \sigma_{yz}^f \sigma_{zz}^f >=< \sigma_{yz}^f \sigma_{xy}^f >=< \sigma_{yz}^f \sigma_{xz}^f >= 0,
\end{aligned}
$$

(18)

where $A = 2k_B\mu T$. In numerical calculations, a Gaussian random number generator is employed to generate five independent Gaussian random variables. Their means and variances satisfy the following equations:

$$
\begin{aligned}
&< m >=< n >= 0, \quad < m^2 >=< n^2 >= \frac{4}{3}A,\\
&< p >=< q >=< r >= 0, \quad < p^2 >=< q^2 >=< r^2 >= A.
\end{aligned}
\tag{19}
$$

By means of m, n, p, q and r, the individual components of the random stress $\sigma_{\alpha\beta}^f$

can be constructed:

$$\sigma_{xx}^f = m, \quad \sigma_{yy}^f = -\frac{1}{2}m + \frac{\sqrt{3}}{2}n, \quad \sigma_{zz}^f = -\frac{1}{2}m - \frac{\sqrt{3}}{2}n,$$
$$\sigma_{xy}^f = p, \quad \sigma_{xz}^f = q, \quad \sigma_{yz}^f = r. \tag{20}$$

2.3 Boundary conditions

During the simulation, boundary conditions are imposed at each time step to determine the distribution functions at boundary nodes. Periodic boundary conditions are applied at the outer boundaries of the computational domain. Furthermore, when handling the interface between the fluid and the particles, quadratic interpolation is employed between fluid and solid nodes to improve the accuracy of the boundary treatment.

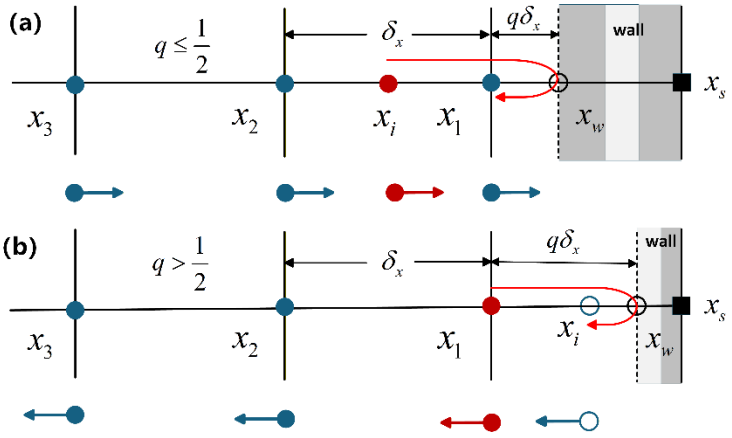


Figure 2: Schematic diagram of the interpolated bounce-back treatment at the fluid-solid interface (a) $q \le 1/2$ and (b) $q > 1/2$

In Figure 2, $\boldsymbol{x}_1$, $\boldsymbol{x}_2$ and $\boldsymbol{x}_3$ are fluid nodes; $\boldsymbol{x}_s$ is a solid node; and $\boldsymbol{x}_w$ is the boundary intersection point on the fluid-solid interface. $\boldsymbol{x}_1$ is the fluid point closest to the solid node; $\boldsymbol{x}_2 = \boldsymbol{x}_1 + \boldsymbol{e}_{\bar{i}}$ and $\boldsymbol{x}_3 = \boldsymbol{x}_2 + \boldsymbol{e}_{\bar{i}}$, where $\boldsymbol{e}_{\bar{i}} = -\boldsymbol{e}_i$; the solid point is $\boldsymbol{x}_s = \boldsymbol{x}_1 + \boldsymbol{e}_i$. The distance between the intersection points of the solid boundary and the fluid-solid interface and the nearest fluid point is given by q, where $q = \frac{|\boldsymbol{x}_1 - \boldsymbol{x}_w|}{|\boldsymbol{x}_1 - \boldsymbol{x}_s|}$. When $q < 1/2$, interpolation is performed before streaming and bounce-back; when $q = 1/2$, a halfway rebound is applied directly; when $q > 1/2$, interpolation is performed after streaming and bounce-back. Moreover, the interaction at the fluid-solid interface is taken into account by adding the force term $3w_i(\boldsymbol{e}_i \cdot \boldsymbol{u}_w)$ to the end of the equation. Combining streaming and collision into a unified operation yields the quadratic interpolation formula as:

$$\begin{cases} f_{\bar{i}}(\boldsymbol{x}_1,t) = q(1+2q)f_i(\boldsymbol{x}_s,t) + (1-4q^2)f_i(\boldsymbol{x}_1,t) - q(1-2q)f_i(\boldsymbol{x}_2,t) + 3\omega_i(\boldsymbol{e}_i\cdot\boldsymbol{u}_w), & q<\dfrac{1}{2} \\ f_{\bar{i}}(\boldsymbol{x},t) = \dfrac{1}{q(1+2q)}f_i(\boldsymbol{x}_s,t) + \dfrac{2q-1}{q}f_{\bar{i}}(\boldsymbol{x}_2,t) - \dfrac{2q-1}{2q+1}f_i(\boldsymbol{x}_3,t) + \dfrac{3\omega_i}{q(2q+1)}(\boldsymbol{e}_i\cdot\boldsymbol{u}_w), & q\geq\dfrac{1}{2} \end{cases} \tag{21}$$

2.4 Particle dynamics

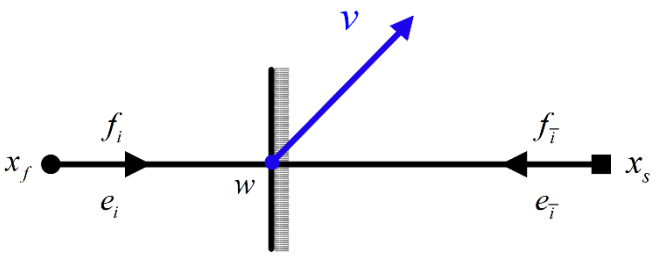


Figure 3: Schematic diagram of the Galilean-invariant momentum exchange method. Points $\boldsymbol{x}_f$ and $\boldsymbol{x}_s$ represent fluid and solid nodes, respectively; the moving boundary intersects the fluid-solid interface at point w; the moving boundary itself has a velocity $\boldsymbol{v}$

Calculating the total force $\boldsymbol{F}_{total}$ and torque $\boldsymbol{T}_{total}$ acting on solid particles is a key step in the lattice Boltzmann method for particulate flow. In this study, the Galilean-invariant momentum exchange scheme proposed by Wen et al.[37] is used. The momentum exchange method employed in the present study is schematically illustrated in Figure 3. To account for the velocity at moving boundaries, the absolute velocity in the momentum exchange scheme is replaced by the relative velocity. Subsequently, the momentum exchange for a fluid-solid boundary line can be expressed as follows:

$$F(\boldsymbol{x}_w) = (\boldsymbol{e}_i - \boldsymbol{u}_w)f_i(\boldsymbol{x}_f,t) - (\boldsymbol{e}_{\bar{i}} - \boldsymbol{u}_w)f_{\bar{i}}(\boldsymbol{x}_s,t). \tag{22}$$

The total force $\boldsymbol{F}_{total}$ and total torque $\boldsymbol{T}_{total}$ are obtained by summing the forces and torques calculated along all fluid-solid interface lines for this particle, respectively. The calculation formulas are as follows:

$$\boldsymbol{F}_{total} = \sum \boldsymbol{F}(\boldsymbol{x}_w), \tag{23}$$

$$\boldsymbol{T}_{tatal} = \sum (\boldsymbol{x}_w - R)\times\boldsymbol{F}(\boldsymbol{x}_w). \tag{24}$$

For rigid particles, the equations of motion are

$$M\frac{d\boldsymbol{U}(t)}{dt}=\boldsymbol{F}(t), \tag{25}$$

$$I\cdot\frac{d\boldsymbol{\Omega}(t)}{dt}+\boldsymbol{\Omega}(t)\times[I\cdot\boldsymbol{\Omega}(t)]=\boldsymbol{T}(t). \tag{26}$$

The displacement and rotation of the particle over time can be calculated using the equations of Newton and Euler[38]. Here, M is the effective mass of the particle; $\boldsymbol{U}(t)$ and $\boldsymbol{\Omega}(t)$ are the translational velocity and angular velocity of the particle, respectively, at time t; $\boldsymbol{F}(t)$ and $\boldsymbol{T}(t)$ are the total force and total torque acting on the particle at time t, respectively; and I is the particle's moment of inertia.

3. Model Validation

3.1 Sedimentation of a sphere in a box

A standard approach for validating the treatment of forces, particle displacements, and boundary conditions is to compare numerical results with an established benchmark experiment, such as that reported by ten Cate et al.[39]. To verify the accuracy of the present numerical model, the classical sedimentation experiment of a spherical particle was first simulated.

The reference sedimentation experiment was conducted by ten Cate et al. in 2002 using a vertical, rigid rectangular container. In this experiment, the rectangular container measured 100 mm in length, 100 mm in width, and 160 mm in height. The sphere was initially positioned on the vertical centerline of the rectangular container, and its bottom was 120 mm above the bottom of the container. The sphere had a diameter of 15 mm and a density of 1120 kg/m^3. The physical parameters for the four sedimentation experiments are shown in Table 1. In our numerical simulation, the flow field dimensions are $100\times100\times160$ grid units, the sphere diameter is 15 grid units, and the relaxation time is set to $\tau=0.6$. Figure 4 shows the time evolution of the sphere's center height relative to the container bottom and its settling velocity for the four cases. Cases 1 and 2 correspond to viscosity-dominated sedimentation at low Reynolds numbers, providing a test of algorithmic stability under low-inertia conditions, whereas Cases 3 and 4 correspond to higher Reynolds numbers and provide a test of computational accuracy under moderate to high inertial conditions. The numerical results are in good agreement with the experimental data, indicating that the present boundary treatment and momentum exchange scheme accurately reproduce the hydrodynamic motion of a settling sphere.

TABLE 1

Physical Parameters for the Sedimentation Experiment

Case	$\rho_f(kg/m^3)$	$\mu_f(mPa{\cdot}s)$	Re
Case 1	970	373	1.5
Case 2	965	212	4.1
Case 3	962	113	11.6
Case 4	960	58	31.9

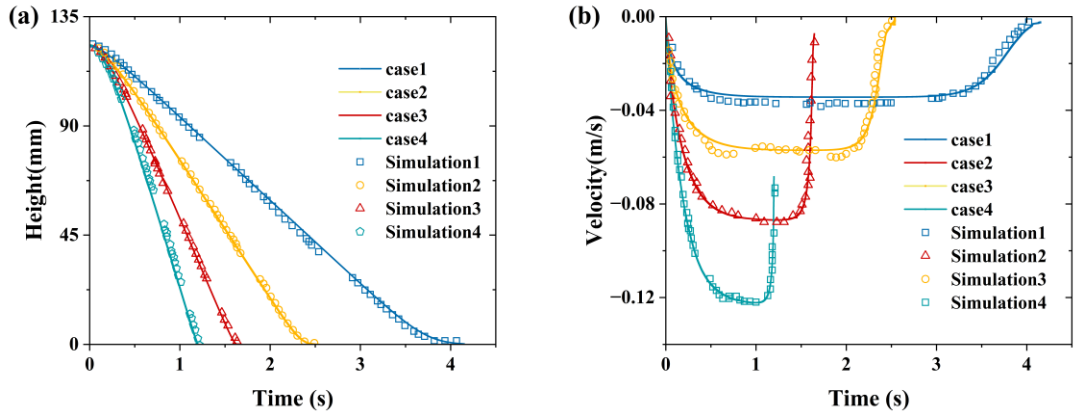


Figure 4: Comparison between the numerical results and the experimental data of ten Cate et al. for a sphere settling in a rectangular container: (a) vertical particle trajectories and (b) settling velocities

3.2 Migration of a sphere in Poiseuille flow

Inertial migration of particles in laminar pipe flow was first observed experimentally by Karnis et al.[40]. Subsequent studies established that the Segré-Silberberg effect[41] arises from inertial lift in the flow. To further demonstrate the validity of our approach, this study simulates the inertial migration of a rigid sphere in Poiseuille flow, specifically the Segré-Silberberg effect. In this experiment, the cylindrical tube has a radius of R = 0.2 cm and the sphere has a radius of r = 0.061 cm. Both the fluid and the sphere have the same density of 1.05 g/cm³. The dynamic viscosity is 1.2 Po, the flow rate of the fluid in the circular tube is 0.0711 cm³/s, and the Reynolds number is 0.198. During the simulation, the radius of the sphere is 9.5 grid units. The pipe length is 256 grid units. The relaxation time τ is 0.65. The pressure difference between the inlet and outlet is 1.677×10^{-5}. This study simulates the migration trajectories of a sphere at two different initial positions, r*/R = 0.21 and

0.66, where r* represents the radial distance from the center of the sphere to the tube centerline. Figure 5 plots the migration trajectories of the sphere at these two initial positions. The numerical results agree well with the experimental data, confirming that the model can accurately reproduce the inertial migration behavior of spherical particles.

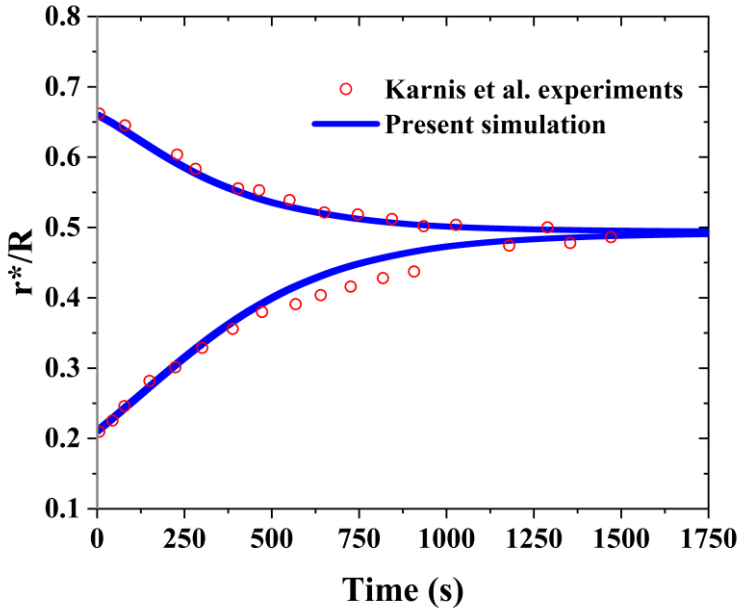


Figure 5: Inertial migration of a sphere in Poiseuille flow

4. Brownian Motion Simulations and Discussion

4.1 Energy equipartition theorem

The energy equipartition theorem provides the fundamental theoretical framework for describing the Brownian motion of microparticles. During Brownian motion, a microparticle continuously exchanges momentum and energy with the surrounding fluctuating fluid. In the early stages, the microparticle gains kinetic energy through collisions and interactions with surrounding fluid molecules. This process continues until the microparticle reaches a state of thermal equilibrium with the fluid. Once thermal equilibrium is reached, the average kinetic energy of the microparticle and that of the fluid molecules are both $3k_BT/2$. Thermal equilibrium represents a dynamic process where particles continuously exchange energy with surrounding fluid molecules. Furthermore, the translational and rotational energies for each degree of freedom of the microparticles are equal, and the average energy in

each degree of freedom is equal to $k_B T/2$, which can be expressed as:

$$< \boldsymbol{U}(0)\boldsymbol{U}(0) >=< \boldsymbol{V}(0)\boldsymbol{V}(0) >=< \boldsymbol{W}(0)\boldsymbol{W}(0) >= k_B T / M, \tag{27}$$

$$< \boldsymbol{\Omega}(0)\boldsymbol{\Omega}(0) >=< \boldsymbol{\Phi}(0)\boldsymbol{\Phi}(0) >=< \boldsymbol{\Psi}(0)\boldsymbol{\Psi}(0) >= k_B T / I, \tag{28}$$

where $\boldsymbol{U}$, $\boldsymbol{V}$, and $\boldsymbol{W}$ represent the translational velocities of the Brownian particle along the x, y and z directions, respectively; $\boldsymbol{\Omega}$, $\boldsymbol{\Phi}$, and $\boldsymbol{\Psi}$ represent the angular velocities of the Brownian particle along the x, y, and z directions, respectively; M and I represent the mass and moment of inertia of the Brownian particle, respectively.

In this study, a small spherical particle is released at the center of a cubic domain, with all external forces neglected so that only Brownian forces arising from thermal fluctuations of the fluid are considered. Here, the Brownian force denotes the random force exerted by the surrounding fluid as a consequence of thermal fluctuations. In the present FLB framework, the Brownian force is not imposed as an external force but emerges from the stochastic stress tensor in the fluid equations, which couples the thermal fluctuations of the fluid to the particle motion through the momentum exchange scheme. The flow field has a size of $100 \times 100 \times 100$ (in lattice units). The sphere has a density of $\rho_p = 2600\, kg/m^3$ and a diameter of $d = 1\, \mu m$. The fluid density is $\rho_f = 1000\, kg/m^3$, its temperature is $T = 293\, K$, and its kinematic viscosity is $\upsilon = 1.01 \times 10^{-6}\, m^2/s$. Initially, the sphere is centered in the domain. Its diameter is resolved by 10 grid units, and the relaxation time is set to $\tau = 1$. Based on this setup, the mean-square velocity (MSV) and mean-square angular velocity (MSA) profiles of the sphere under the three different velocity models are plotted in Figure 6. Figure 6 presents the time histories of MSV and MSA for the spherical particle under the D3Q15, D3Q19, and D3Q27 FLB models (top, middle, and bottom rows, respectively). The results are plotted as functions of the normalized time t/τ_υ. Here, $\tau_\upsilon = a^2/\upsilon$, where a is the particle radius and υ is the kinematic viscosity of the fluid. This time scale characterizes the viscous diffusion over the particle size.

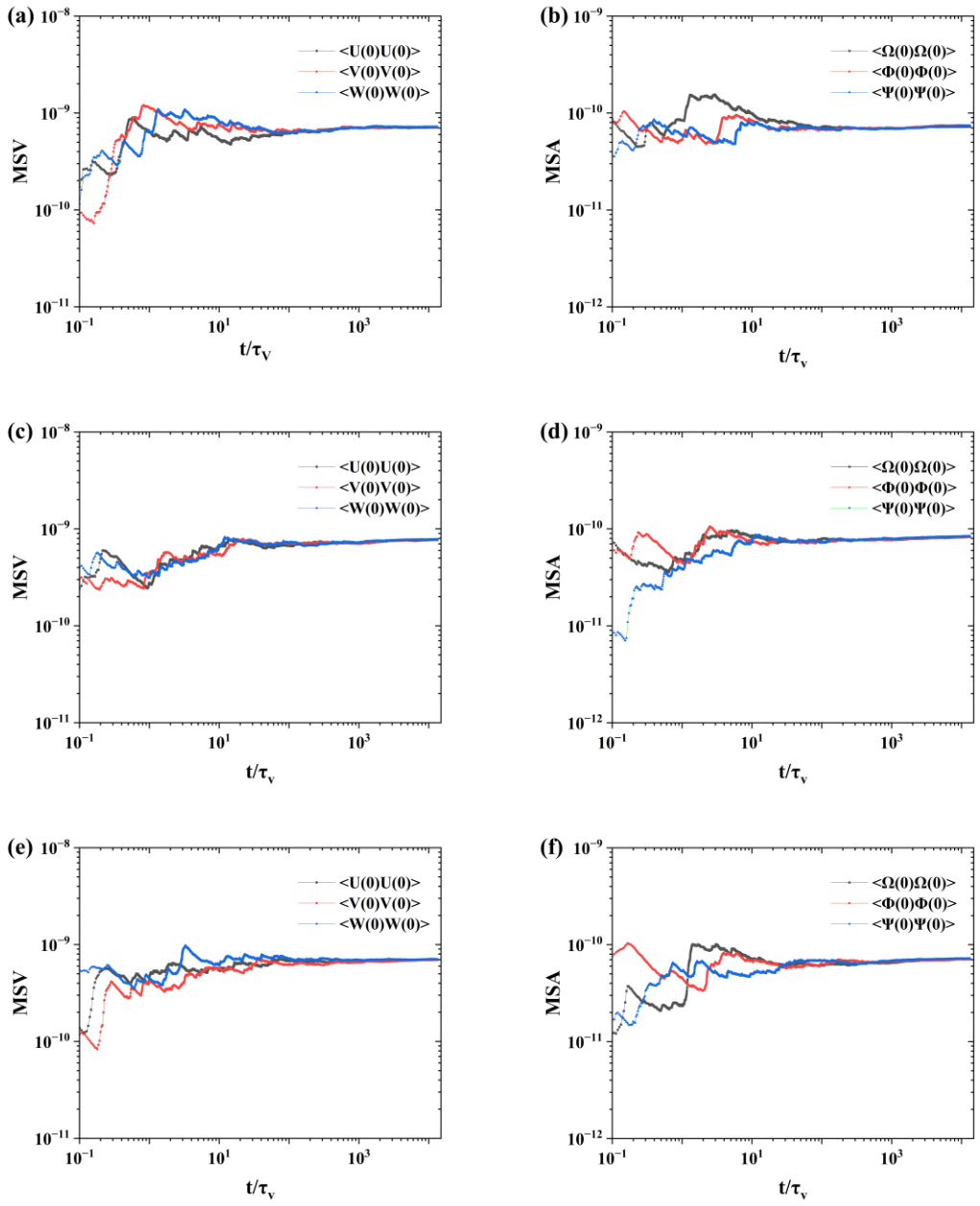


Figure 6: The MSV and MSA for the three FLB models of the sphere undergoing Brownian motion. From top to bottom, the first row (a, b) shows our baseline results for the conventional D3Q15 model; the second row (c, d) shows results using the D3Q19 fluctuation model; and the third row (e, f) shows results using the D3Q27 fluctuation model

For comparison with the equipartition theorem predictions, the MSV and MSA in each Cartesian direction are further normalized by their corresponding theoretical equilibrium values, as defined in Eqs. (27) and (28). Specifically, the normalized MSV and MSA are defined as

$$\begin{cases} < \boldsymbol{U}(0)\boldsymbol{U}(0) >^{*} = << \boldsymbol{U}(0)\boldsymbol{U}(0) > /(K_B T / M) \\ < \boldsymbol{V}(0)\boldsymbol{V}(0) >^{*} = < \boldsymbol{V}(0)\boldsymbol{V}(0) > /(K_B T / M) \\ < \boldsymbol{W}(0)\boldsymbol{W}(0) >^{*} = < \boldsymbol{W}(0)\boldsymbol{W}(0) > /(K_B T / M) \end{cases}, \tag{29}$$

$$\begin{cases} < \boldsymbol{\Omega}(0)\boldsymbol{\Omega}(0) >^{*} = < \boldsymbol{\Omega}(0)\boldsymbol{\Omega}(0) > /(K_B T / J) \\ < \boldsymbol{\Phi}(0)\boldsymbol{\Phi}(0) >^{*} = < \boldsymbol{\Phi}(0)\boldsymbol{\Phi}(0) > /(K_B T / J) \\ < \boldsymbol{\Psi}(0)\boldsymbol{\Psi}(0) >^{*} = < \boldsymbol{\Psi}(0)\boldsymbol{\Psi}(0) > /(K_B T / J) \end{cases}. \tag{30}$$

According to the energy equipartition theorem, the normalized translational and angular velocity variances defined in Eqs. (29) and (30) should approach unity after the system reaches thermal equilibrium. Figure 7 presents the time evolution of these normalized quantities for the D3Q15, D3Q19, and D3Q27 FLB models. The horizontal dashed line denotes the theoretical equipartition value of unity.

As shown in Figure 7, the normalized translational and angular velocity variances predicted by all three models gradually approach unity after the initial transient, indicating that the thermal energy prescribed by FDT is correctly transferred to the particle. Here, the thermal energy refers to the energy scale $k_B T$ prescribed by FDT, which corresponds to an average of $k_B T/2$ per degree of freedom according to the equipartition theorem (Eqs. (27) and (28)). The results in the three directions also converge toward comparable values, demonstrating that the simulated fluctuations are approximately isotropic. Compared with the D3Q15 model, the D3Q19 and D3Q27 models exhibit smaller directional deviations and more stable fluctuations around the theoretical equilibrium value, which supports the effectiveness of relaxing the strict symmetry constraint imposed on opposite lattice directions.

In addition to accuracy, the computational cost of the three FLB models is also worth considering. The proposed random difference construction per lattice unit introduces only marginal extra operations, such as random number generation and simple additions, so the overall cost is dominated by the standard collision and streaming steps. Consequently, the D3Q19 model requires roughly 30% more computation than D3Q15, and D3Q27 roughly 40% more than D3Q19, consistent with their velocity-direction counts. This cost increase is acceptable given the improved accuracy obtained with D3Q19 and D3Q27, especially for D3Q27.

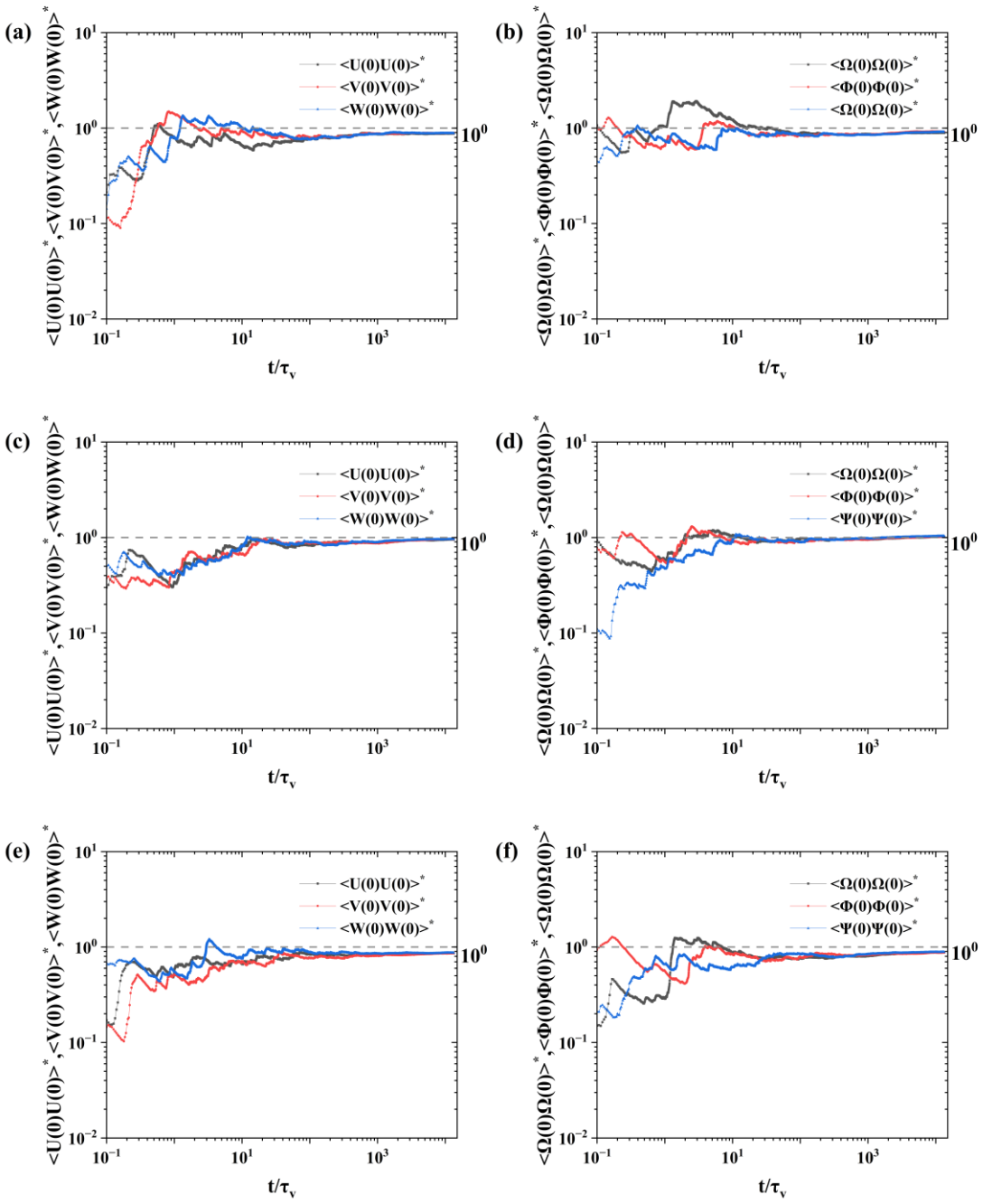


Figure 7: Time evolution of the normalized translational and angular velocity variances of a Brownian sphere predicted by the D3Q15, D3Q19, and D3Q27 FLB models. Panels (a) and (b) show the D3Q15 results, panels (c) and (d) show the D3Q19 results, and panels (e) and (f) show the D3Q27 results. The left and right columns correspond to the translational and angular velocity variances, respectively. The horizontal dashed line denotes the theoretical equipartition value of unity

4.2 Mean-square displacement and diffusion coefficient

The diffusion coefficient D quantifies the rate of diffusion through a medium. A larger D indicates faster diffusion. According to Einstein's 1905 theory[42] of Brownian motion, the diffusion coefficient D can be obtained from the MSD of the particles via $D = \lim_{\Delta t \to \infty} < \Delta r^2 > /(2d\Delta t)$, where $< \Delta r^2 >$ is the MSD over a lag time Δt, and d denotes the spatial dimensionality ($d = 1,\ 2,\ or\ 3$). In the long-time limit, as the particle motion transitions into the diffusive regime, the MSD grows linearly with time, and the value of D evaluated from this relation converges to a constant plateau. Before calculating D, the MSD of the particles must first be evaluated. It is defined as follows:

$$MSD(\Delta t) = <| \boldsymbol{r}(t + \Delta t) - \boldsymbol{r}(t) |^2 > . \tag{31}$$

The MSD is computed from the particle trajectory as:

$$MSD(\Delta t) = \frac{1}{N-n} \sum_{i=0}^{N-n-1} | \vec{\boldsymbol{r}}_{(\cdot)} \quad \vec{\boldsymbol{r}}_{(\cdot)} | \tag{32}$$

Here, Δt denotes the observation interval; t_i denotes different start times; $\vec{r}(t)$ represents the position of the Brownian particle at time t; N is defined as the total number of positions recorded for the Brownian particle, and n denotes the number of intervals corresponding to the time difference. According to Einstein's theory of Brownian motion, the MSD of a spherical particle undergoing Brownian motion and the simulated value of D are determined by the Einstein-Smoluchowski[43, 44] equation, which is expressed as follows:

$$< \boldsymbol{r}(\Delta t)^2 >= 2dD\Delta t. \tag{33}$$

Here, d represents the dimension. When d is 2 or 3, it corresponds to two-dimensional and three-dimensional cases, respectively. In the context of the sphere simulation described in this paper, the formula takes the following form:

$$< r(\Delta t)^2 >= 6D\Delta t. \tag{34}$$

The theoretical value of D is determined using the Stokes-Einstein[45] equation, which is as follows:

$$D = \frac{k_B T}{6\pi\mu a}. \tag{35}$$

To determine the random stress components via the FDT and thereby compute the fluctuation terms, the term k_BT in the equation must be dimensionless. In this process, dimensional analysis in terms of mass, length, and time is used for this purpose. When the particle diameter D_p, the fluid density ρ , and the kinematic viscosity υ are taken as the reference physical quantities, the following scaling relations are established:

$$\begin{cases} D_p = D^{LU} L \\ \upsilon = \upsilon^{LU} \dfrac{L^2}{T} \\ \rho = \rho^{LU} \dfrac{M}{L^3} \end{cases}, \tag{36}$$

where D^{LU} denotes the number of lattice units corresponding to the particle diameter in the lattice space, ρ^{LU} is the fluid density on the lattice, υ^{LU} is the kinematic viscosity of the lattice fluid, and M is the dimensional scale of the mass. From the above relations, the SI-unit expressions for length, mass, and time in the lattice space are obtained as:

$$\begin{cases} L = \dfrac{D_p}{D^{LU}} \\ T = \dfrac{\upsilon^{LU}}{\upsilon} (\dfrac{D_p}{D^{LU}})^2 \\ M = \dfrac{\rho}{\rho^{LU}} (\dfrac{D_p}{D^{LU}})^3 \end{cases} \tag{37}$$

Here, L and T denote the dimensional scales of length and time, respectively. Equivalently, from the kinetic energy formula $E = \frac{1}{2}mv^2$ with $v = L/T$, the same result is obtained. The defining relation of energy gives

$$E = M(\frac{L}{T})^2. \tag{38}$$

Here, M represents the mass dimension and E represents the energy dimension. Dimensional conversion gives k_BT in the simulation as approximately 1.10155×10^{-6}. Using the setup described in Section 4.1, the MSD of the sphere in each direction and the total MSD as a function of the observation interval are computed for the three velocity models. The D3Q15 simulations are performed using the original FLB model of Nie et al. as a baseline, whereas the D3Q19 and D3Q27 simulations are conducted with our newly proposed formulations, given by Eqs. (16) and (17), respectively. In our simulations, each case was integrated for 5×10^6

lattice time steps. The first 3×10^5 steps were discarded as a transient period to ensure thermal equilibrium. Thereafter, particle positions and velocities were recorded at every time step. The MSD was calculated using time averaging over all possible starting times according to Eq. (32), and D was obtained from the linear slope of the MSD curve in the long-time regime. GPU parallelization was adopted to accelerate the simulations owing to the large computational domain and the long flow evolution time; the sampling and averaging procedures remained unchanged.

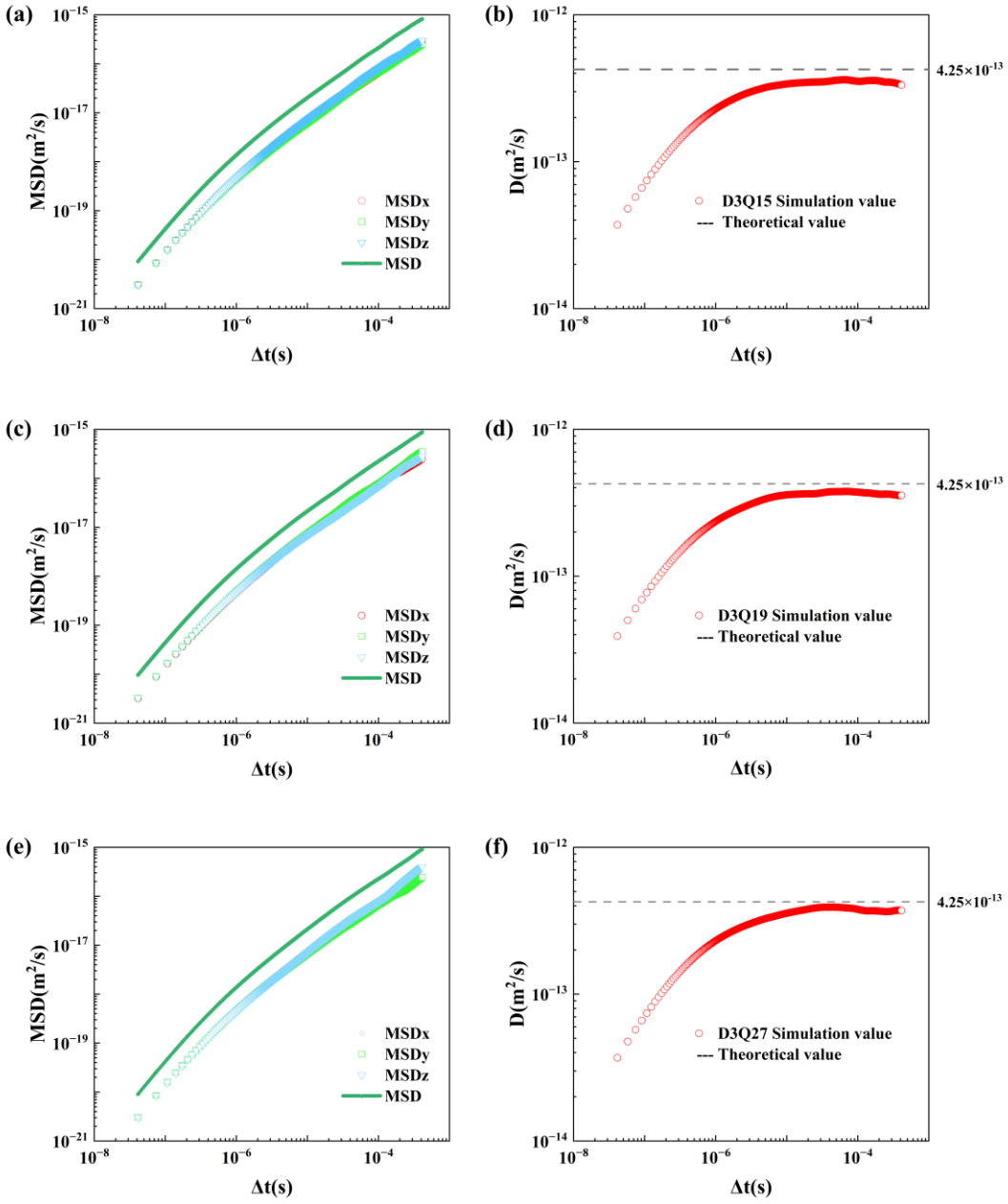


Figure 8: Variation of the MSD and D of the sphere with observation time Δt under the three FLB models. From top to bottom, the first row (a, b) shows our baseline results for the

conventional D3Q15 model. The second row (c, d) shows results using the D3Q19 FLB model. The third row (e, f) shows results using the D3Q27 FLB model

As shown in Figure 8, the MSD values in the three directions are consistent with each other within the statistical uncertainty, which reflects the expected isotropic behavior of the spherical particle and provides further evidence for the capability of the FLB method in simulating Brownian motion. Figure 8 plots the simulated D_s of the sphere as a function of observation time Δt for the three FLB models. The dashed line in the figure represents the theoretical value of D_t determined using the Stokes-Einstein equation, which is approximately $4.25 \times 10^{-13}\ m^2/s$. The red circles represent D_s at different observation times, calculated using the formula, which ultimately fluctuate around $3.55 \times 10^{-13}\ m^2/s$, $3.65 \times 10^{-13}\ m^2/s$, and $3.70 \times 10^{-13}\ m^2/s$, respectively. To provide a quantitative comparison with the theoretical prediction, the present work summarizes in Table 2 the final simulated diffusion coefficients D_s alongside the Stokes-Einstein value $D_t = 4.25 \times 10^{-13}\ m^2/s$ and the corresponding relative errors, defined as $\frac{|D_t - D_s|}{D_t} \times 100\%$. The results show that the D3Q19 and D3Q27 FLB models proposed in this work yield a D_s closer to the free-diffusion value D_t than the conventional D3Q15 FLB model, corresponding to a reduction in the relative error of approximately 3%. This indicates that the proposed method is more reliable than the baseline model. Because the conversion of k_BT from physical units to lattice units preserves the energy scale only approximately, the fluctuation intensity in the simulation may not exactly match the prescribed thermodynamic temperature. Consequently, the final steady-state D_s in our simulations always exhibits slight deviations from D_t. Therefore, a correction factor is introduced to further compare the differences among the three models.

To further justify the choice of the amplitude coefficient in the random intervals for the free variables in Eqs. (16) and (17), a series of numerical tests was conducted with different values of the coefficient β, with the fluctuation range defined as $[-\beta|\xi_{i+3}|,\ \beta|\xi_{i+3}|]$. The corresponding simulated diffusion coefficients of the spherical particle are summarized in Tables 3 and 4. Over this fourfold range (β = 1/20 to 1/5), the relative spread of D_s, defined as $\frac{D_{s,max} - D_{s,min}}{D_{s,min}}$, is at most about 3.4% for D3Q19 and 1.4% for D3Q27, with no systematic monotonic dependence on β; the results are therefore insensitive to the precise value of β within this range. The value β = 0.10 lies within this insensitive range and is adopted as a representative

value rather than a fitted parameter, and the same value is used for both models to ensure a fair comparison.

TABLE 2

Comparison of the simulated diffusion coefficients with the theoretical Stokes-Einstein prediction for the three FLB models.

Model	Simulated D_s	Theoretical D_t	Relative error
D3Q15	3.55×10^{-13}	4.25×10^{-13}	16.5%
D3Q19	3.65×10^{-13}	4.25×10^{-13}	14.1%
D3Q27	3.70×10^{-13}	4.25×10^{-13}	12.9%

TABLE 3

Simulated diffusion coefficient D_s of the spherical particle for different values of the amplitude coefficient β in the D3Q19 FLB model.

β	D_s(×10⁻¹³ m²/s) for D3Q19
1/5	3.54
1/10	3.65
1/15	3.56
1/20	3.53

TABLE 4

Simulated diffusion coefficient D_s of the spherical particle for different values of the amplitude coefficient β in the D3Q27 FLB model.

β	D_s(×10⁻¹³ m²/s) for D3Q27
1/5	3.68
1/10	3.70
1/15	3.73
1/20	3.71

4.3 Fluctuation intensity correction factor

A standard measure of FLB performance for Brownian motion is to compare the D_s with D_t. Nevertheless, due to numerical discretization including velocity discretization, errors in space-time integration, the accuracy of momentum exchange in the boundary treatment scheme, and the effects of finite system size, the fluctuation intensity driven by the k_BT, which is directly input via strict physical dimensional

transformation, often fails to yield a simulated D_s that perfectly matches the theoretical value D_t. This discrepancy reflects the inherent numerical dissipation or amplification that arises when the model maps the FDT of a continuous medium to a discrete lattice system.

To quantify this discrepancy and systematically evaluate the three FLB models, this study introduces a fluctuation intensity correction factor α. The core idea is to define the effective thermodynamic temperature actually acting on the random motion of particles as $T_{eff} = \alpha T$, meaning that the corresponding effective thermal energy is $\alpha k_B T$. With fluid dynamic viscosity η, particle diameter d, and all other parameters remaining strictly constant, this paper adjusted the value of α so that the long-term D_s obtained from the simulation matches D_t within statistical uncertainty. In this case, the magnitude of the required correction factor α directly reflects the accuracy of the FLB model in simulating Brownian motion. A value of α closer to 1 indicates that the discretization error of the model is smaller, that its inherent stochastic dynamic behavior is more consistent with continuous theory, and that the model demonstrates better theoretical consistency or physical accuracy. The correction factor should not be regarded as a universal physical constant, because it may depend on the grid resolution, domain size, particle size, boundary treatment, and statistical sampling procedure.

Based on this approach, different correction factors are introduced during the simulation to account for various FLB models, ensuring that as the observation time Δt increases, D_s of the sphere undergoing Brownian motion matches D_t. Similarly, the D3Q15 simulations are performed using the original D3Q15 FLB model as a baseline, whereas the D3Q19 and D3Q27 simulations are conducted with our newly proposed formulations, given by Eqs. (16) and (17), respectively. In this simulation, the required correction factors α for the three models are 1.22, 1.20, and 1.10 for the D3Q15, D3Q19, and D3Q27 models, respectively, as listed in Table 5. The correction factor α for each model is calibrated as follows. For a given velocity model, α is varied systematically and the corresponding long-time diffusion coefficient $D_s(\alpha)$ is computed. The optimal value is taken as the one satisfying $D_s(\alpha) = D_t$ within statistical uncertainty, where $D_t = k_B T/6\pi\eta a$. This yields α = 1.22, 1.20, and 1.10 for D3Q15, D3Q19, and D3Q27, respectively. With all other simulation conditions remaining identical, the three models are compared by varying only the fluctuation intensity $k_B T$ and the FLB models. Subsequently, variations in the MSD and D_s of

the sphere are obtained for different observation intervals Δt. Figure 9 shows the corrected results for the D3Q15, D3Q19, and D3Q27 FLB models (top to bottom), which require correction factors of approximately 1.22, 1.20, and 1.10, respectively, to recover the D_t.

The correction factor α serves as a quantitative measure of the combined numerical error inherent in each velocity model, including finite-size effects, discretization errors, and the fidelity of the stochastic stress representation. A smaller α indicates that the model introduces less deviation from the theoretical FDT. The D3Q19 and D3Q27 FLB models, with their richer sets of discrete velocities, provide a more isotropic representation of the stress tensor and more accurate momentum exchange, thereby requiring smaller empirical corrections. Thus, the ranking of α not only calibrates the simulations but also quantifies the relative accuracy of the three formulations. The D3Q27 model, requiring the smallest correction, offers the highest fidelity among the models tested.

TABLE 5

Correction factors required for each model

Model	**Uncorrected D**	**α**	**Corrected D**
D3Q15	3.55×10^{-13}	1.22	Approx.4.25×10^{-13}
D3Q19	3.65×10^{-13}	1.20	Approx.4.25×10^{-13}
D3Q27	3.70×10^{-13}	1.10	Approx.4.25×10^{-13}

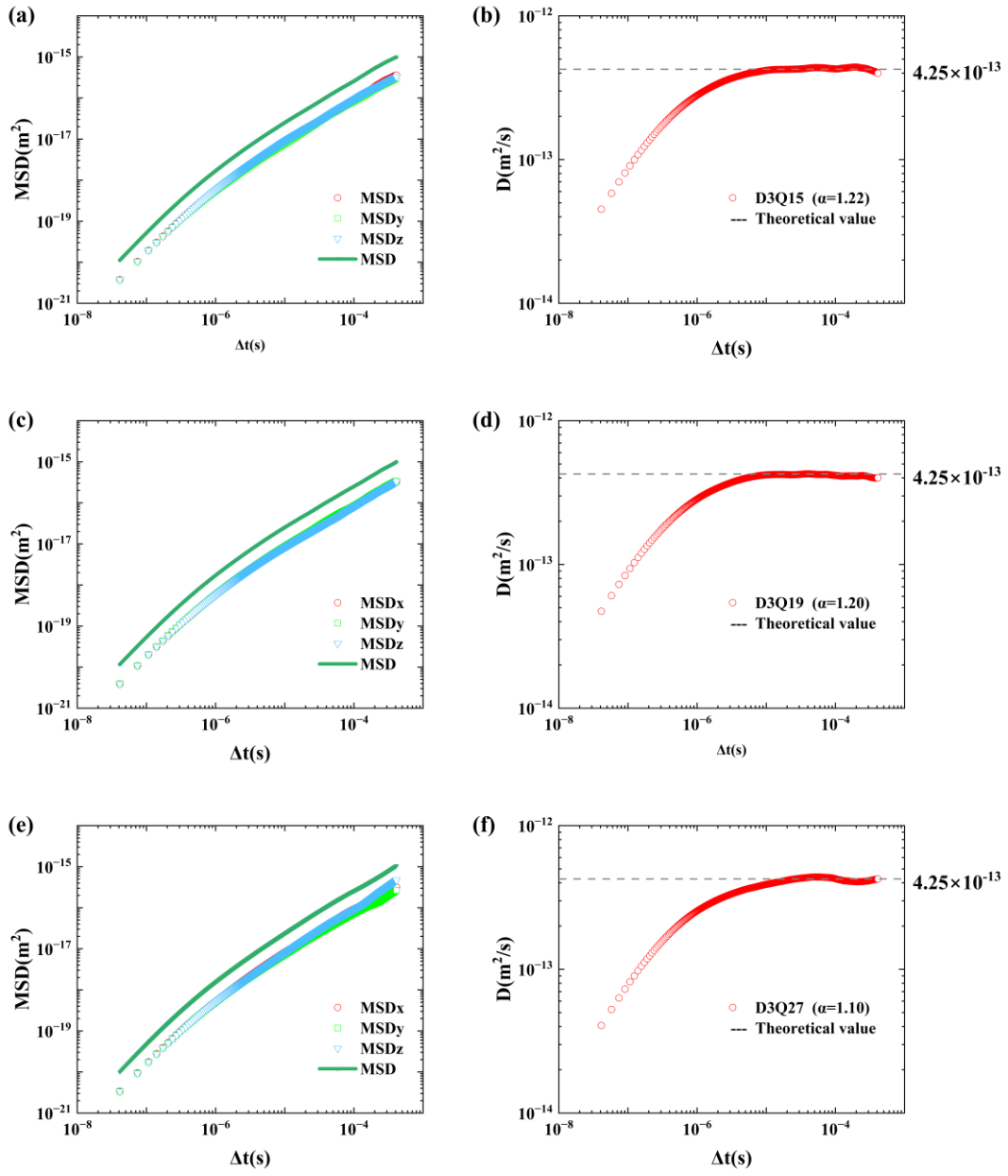


Figure 9: After applying the correction factor, the MSD and D of the sphere as a function of observation time Δt are shown. The figure is arranged in three rows from top to bottom: (a, b) baseline results for the conventional D3Q15 FLB model, (c, d) results using the D3Q19 fluctuation model, and (e, f) results using the D3Q27 fluctuation model

5. Conclusions

This study proposes an FLB model with independent directional stochastic

fluctuations to simulate the Brownian motion of microparticles. A fluctuation term is incorporated into the standard lattice Boltzmann evolution equation, and the Chapman-Enskog multiscale expansion is employed to derive the relationship between the stochastic stress tensor and the fluctuation terms by comparison with the Navier-Stokes equations. Based on mass and momentum conservation and appropriate closure assumptions, explicit fluctuation terms are constructed for the D3Q19 and D3Q27 FLB models. To better represent the inherent stochasticity of Brownian motion, the conventional strict symmetry assumption for the fluctuation terms in opposite lattice directions is relaxed. The proposed formulation constrains only the sum of each opposite-direction pair and introduces random variables to control their differences.

The effectiveness of the proposed method is evaluated through simulations of the Brownian motion of a spherical particle. The energy equipartition results show that the translational and rotational velocity fluctuations predicted by the three models are consistent with the prescribed thermal equilibrium statistics. Analysis of the MSD and D further demonstrates that the D3Q19 and D3Q27 models provide closer agreement with the Stokes-Einstein prediction than the conventional D3Q15 model. This corresponds to an approximately 3 % lower relative error than the baseline D3Q15 FLB model. A model-dependent fluctuation intensity correction factor α is also introduced to quantify the empirical calibration required under the present computational conditions. The smaller correction factors α required by the D3Q19 and D3Q27 models, particularly the D3Q27 formulation, indicate that the proposed constructions reproduce the target Brownian diffusion behavior with less empirical adjustment than the conventional symmetric formulation.

Although the present method has been validated for the Brownian motion of a single spherical particle, its applicability to more complex systems remains largely unexplored. Future work will first aim to establish a more systematic derivation of the fluctuation terms from the statistical covariance constraints inherent to fluctuating hydrodynamics, while systematically quantifying the sensitivity of the proposed models to key physical and numerical parameters. Building upon this foundation, the framework incorporating independent directional stochastic fluctuations will be extended to multicomponent gas mixtures by reformulating the fluctuation-dissipation relation to account explicitly for interspecies interactions. The methodology will then be further generalized to multiparticle systems to incorporate hydrodynamic

interactions and interparticle collisions. These extensions will provide a rigorous assessment of the robustness and generalizability of the proposed framework and ultimately establish a versatile modeling tool for the simulation of complex microscale flows.

Acknowledgments

This work was supported by the National Natural Science Foundation of China (Grant Nos. 12562025, 12272100) and Innovation Project of Guangxi Graduate Education (Grant No. XYCS2026105, XYCBZ2024026, YCBZ2026106), and Guangxi Collaborative Innovation Center of Multisource Information Integration and Intelligent Processing.

References

[1] Wang W, Balcerek M, Burnecki K, Chechkin A V, Janušonis S, Ślęzak J, Vojta T, Wyłomańska A and Metzler R 2023 *Phys. Rev. Res.* **5** L032025.

[2] Wang W, Metzler R and Cherstvy A G 2022 *Phys. Chem. Chem. Phys.* **24** 18482.

[3] Boynewicz J, Thumann M C and Raizen M G 2026 *Sci. Adv.* **12** eaeb4579.

[4] Guo T, Bulin C, Li C, Xin G, Bao J and Song J 2025 *Sep. Purif. Technol.* **354** 128867.

[5] Zhang D, Liu W, Feng L, Feng Y, Yu Y, Cheng T, Han D and Li H 2025 *Research (Wash.)* **8** 0856.

[6] Zöttl A and Stark H 2023 *Annu. Rev. Condens. Matter Phys.* **14** 109.

[7] Mekuye B and Abera B 2023 *Nano Sel.* **4** 486.

[8] Li W 2022 *J. Sol. Energy Eng.* **144** 021011.

[9] Gürsel H, Mangut M and Sucu E 2025 *Class. Quantum Grav.* **42** 135015.

[10] Schalkers M A and Möller M 2024 *Comput. Fluids* **285** 106453.

[11] Samanta R, Chattopadhyay H and Guha C 2022 *Comput. Mater. Sci.* **206** 111288.

[12] Wang B, Meng Z, Zhao Y and Yang Y 2025 *npj Quantum Inf.* **11** 196.

[13] Korb H, Bastin J, Asmuth H and Ivanell S 2026 *Wind Energy Sci.* **11** 983.

[14] Muñiz-Chicharro A, Votapka L W, Amaro R E and Wade R C 2023 *Wiley Interdiscip. Rev. Comput. Mol. Sci.* **13** e1649.

[15] Elfring G J and Brady J F 2022 *J. Fluid Mech.* **952** A19.

[16] Hang Y and Monica O D L C 2023 *Phys. Rev. Fluids* **8** 054101.

[17] Pacheco-Pozo A, Balcerek M, Wyłomanska A, Burnecki K, Sokolov I M and Krapf D 2024 *Phys. Rev. Lett.* **133** 067102.

[18] Vroylandt H 2022 *Europhys. Lett.* **140** 62003.

[19] Gopalakrishnan S, Mcculloch E and Vasseur R 2026 *Phys. Rev. X* **16** 011024.

[20] Knani S, Khemis I B, Fuhr A C F P, Lefi N, Mahmoud S A, Dotto G L, Alenazi A and Selmi R 2025 *Sci. Rep.* **15** 14238.

[21] Adhikari R, Stratford K, Cates M and Wagner A 2005 *EPL.* **71** 473.

[22] Dünweg B, Schiller U D and Ladd A J 2007 *Phys. Rev. E Stat. Nonlin. Soft Matter Phys.* **76** 036704.

[23] Nie D M and Wang C B 2020 *Therm. Sci.* **24** 3707.

[24] Giorgini L T, Falasca F and Souza A N 2025 *Proc. Natl. Acad. Sci. U.S.A.* **122** e2509578122.

[25] Dubois F, Boghosian B M and Lallemand P 2023 *Comput. Fluids* **266** 106036.

[26] Krishnakanth D and Lakshminarayana P 2026 *Mod. Phys. Lett. B* **40** 2650028.

[27] Alazard T and Zuily C 2024 *SIAM J. Math. Anal.* **56** 5285.

[28] Baatar L, Mostaghimi P, Yuan M, Armstrong R T, Adler L, Canbulat I, Si G, Gaidarov B and Jing Y 2023 *Int. J. Coal Geol.* **265** 104155.

[29] Zendehroud S, Daldrop J O, Von Hansen Y, Kiefer H and Netz R R 2024 *Phys. Rev. E* **110** 064610.

[30] Huang Q, Chen Y and Yong W A 2023 *J. Sci. Comput.* **95** 80.

[31] Qian Y H, D'humières D and Lallemand P 1992 *EPL.* **17** 479.

[32] Dektor A and Einkemmer L 2026 *J. Comput. Phys.* **547** 114515.

[33] Yao S, Fei F, Luan P, Jun E and Zhang J 2023 *Phys. Fluids* **35** 037102.

[34] Dou H S 2025 *Phys. Fluids* **37** 084131.

[35] Eyink G L and Peng L 2025 *Nonlinearity* **38** 085011.

[36] Nie D M and Lin J Z 2009 *Particuology* **7** 501.

[37] Wen B, Zhang C, Tu Y, Wang C and Fang H 2014 *J. Comput. Phys.* **266** 161.

[38] Luo Y, Yu H, Zhang H and Zhou Y 2024 *IEEE Trans. Syst. Man Cybern.: Syst.* **54** 2266.

[39] Ten Cate A, Nieuwstad C, Derksen J J and Van Den Akker H 2002 *Phys. Fluids* **14** 4012.

[40] Karnis A, Goldsmith H and Mason S 1963 *Nature* **200** 159.

[41] Jin D, Park J I, You J B, Kim Y, Lee H and Kim J M 2025 *J. Fluid Mech.* **1004** A5.

[42] Škvarla J 2024 *Arch. Hist. Exact Sci.* **78** 833.

[43] Marian V S 1906 *Ann. Phys. (Berlin)* **326** 756.

[44] Evangelista L, Lenzi E, Barbero G and Scarfone A 2024 *Phys. A: Stat. Mech. Appl.* **635** 129491.

[45] Berkowicz S and Perakis F 2021 *Phys. Chem. Chem. Phys.* **23** 25490.